Lattice sites of ion-implanted Mn, Fe and Ni in 6H-SiC

A R G Costa[1], U Wahl[1], J G Correia[1], E David-Bosne[1], L M Amorim[2], V Augustyns[2], D J Silva[3], M R da Silva[4], and L M C Pereira[2]

1) Centro de Ciências e Tecnologias Nucleares, Instituto Superior Técnico, Universidade de Lisboa, E. N. 10 ao km 139, 2695-066 Bobadela LRS, Portugal

2) KU Leuven, Instituut voor Kern-en Stralingsfysica, 3001 Leuven, Belgium

3) IFIMUP and IN-Institute of Nanoscience and Nanotechnology, Departamento de Física e Astronomia da Faculdade de Ciências da Universidade do Porto, 4169-007 Porto

4) Centro de Física Nuclear da Universidade de Lisboa, 1749-016 Lisboa, Portugal

E-mail: angelo@ctn.tecnico.ulisboa.pt

Abstract. Using radioactive isotopes produced at the CERN-ISOLDE facility, the lattice location of the implanted transition metal (TM) ions ^{56}Mn, ^{59}Fe and ^{65}Ni in *n*-type single-crystalline hexagonal 6H-SiC was studied by means of the emission channeling technique. TM probes on carbon coordinated tetrahedral interstitial sites (T_C) and on substitutional silicon sites ($S_{Si,h+k}$) were identified. We tested for but found no indication that the TM distribution on S_{Si} sites deviates from the statistical mixture of 1/3 hexagonal and 2/3 cubic sites present in the 6H crystal. The TM atoms partially disappear from T_C positions during annealing at temperatures between 500 °C and 700 °C which is accompanied by an increase on S_{Si} and random sites. From the temperature associated with these site changes, interstitial migration energies of 1.7-2.7 eV for Mn and Ni, and 2.3-3.2 eV for Fe were estimated. TM lattice locations are compared to previous results obtained in 3C-SiC using the same technique.

Keywords: emission channeling, lattice location, ion implantation, 6H silicon carbide, transition metals, manganese, nickel, iron

1. Introduction

Silicon carbide (SiC) is a IV-IV binary compound semiconductor with strong chemical bonds between silicon and carbon atoms. As a result, SiC is a chemically inert material of high hardness and high thermal conductivity with a wide bandgap energy (ranging from 2.39 eV for 3C-SiC to 3.02 eV for 6H-SiC to 3.26 eV for 4H-SiC crystals) and high breakdown electric field, suitable to be used in high-power or high-frequency applications and high-radiation environments [1-6]. Although Si is still the most commonly used semiconductor for

power devices today, based on technology developed in recent decades it is likely to be outperformed by SiC due to its superior physical and chemical properties.

SiC is known since the beginning of the 20th century but its physical and chemical stability made high quality crystal growth very difficult, which hindered the development of SiC-based technology. Also the characteristics of SiC to easily form many different crystal structures with different stacking sequence along a particular crystallographic direction, called polytypism (cf reference [4] for a good introduction into the subject), has also been an obstacle to grow electronic-grade single crystals. While more than 200 different SiC polytypes are known, the polytype that is of major interest for applications is hexagonal 4H, while hexagonal 6H and cubic 3C are to lesser extent also used [2-3, 5-6]. 3C-SiC represents a pure cubic structure, whereas 4H- and 6H-SiC are formed by alternating hexagonally and cubically coordinated Si-C bilayers. In 4H-SiC, hexagonal and cubic bilayers follow one after the other while in 6H-SiC, a hexagonal bilayer follows after two cubic bilayers. From these three polytypes only 4H- and 6H-SiC are produced in the form of large area wafers. 3C-SiC wafers are currently not yet commercially available but heteroepitaxial 3C layers are grown on various substrate materials such as Si, with the disadvantage of being highly stressed due to the 20% lattice mismatch [7], or on 6H-SiC with the advantages of perfect lattice match and identical chemical properties [4]. Nevertheless, despite significant progress in producing device-grade 3C epilayers in recent years, it is still necessary to further reduce the structural defects during crystal growth before this polytype becomes also an option for more widespread use in certain types of devices where a smaller bandgap than in the hexagonal polytypes would be beneficial [7]. Irrespective of the SiC polytype, nitrogen or phosphorus are employed for *n*-type while aluminium or boron are used for *p*-type doping [1-3, 6, 8]. Substitutional nitrogen occupies carbon sites, whereas aluminium, phosphorus and boron prefer the silicon sublattice. In 4H- and 6H-SiC the dopant ionization energies also depend on whether the site coordination is hexagonal (*h*) or cubic (*k*) [6, 8], hence it is not only of interest to distinguish between possible site preferences for Si *vs* C sublattice, but also between (*h*) *vs* (*k*).

Transition metal (TM) impurities are also frequently found in bulk SiC samples due to the production processes normally employed [9-10] but it is not clear where those TMs are located, either incorporated in substitutional or interstitial sites or forming complexes with other atoms and/or with intrinsic structural defects. We have recently addressed this issue [11] in 3C-SiC implanted with the radioactive TM impurities ^{56}Mn, ^{59}Fe and ^{65}Ni, by means of the β^- Emission Channeling (EC) technique. The EC method [12-13] is based on the observation of anisotropic β^- emission when the radioactive probe atoms are embedded in single crystals. The resulting experimental angular emission patterns are then compared with many-beam simulations [12] for emitter atoms on substitutional silicon and carbon sites and various interstitial positions, which permits identifying and quantifying the probe atom site occupancy. In the present work the lattice locations of the radioactive isotopes ^{56}Mn, ^{59}Fe and ^{65}Ni implanted into *n*-type 6H-SiC single crystals were investigated as function of the annealing temperature. For that purpose we have performed detailed many-beam simulations for different types of substitutional and a variety of interstitial sites in 6H-SiC. While many-beam simulations were previously applied to analyze the lattice location of the rare earth isotope ^{169}Tm in 6H-SiC [14] at that time only substitutional Si sites were considered, and without any distinction between (*h*) and (*k*) sites.

2. Experiment

Three nitrogen doped *n*-type 6H-SiC single crystal samples were cut from a *c*-axis oriented wafer obtained from CrysTec GmbH. The reason why we used the 6H polytype is that by the time the samples were purchased (in 2004) 6H bulk wafers were commonly available in better structural quality than 4H. Mass separated and chemically clean beams of radioactive isotopes were provided by the on-line isotope separator ISOLDE-CERN facility [15]. The transition metal radioisotopes were produced by fission of uranium carbide UC_2 targets, induced by 1.4 GeV proton beams from the CERN PS-BOOSTER, followed by chemically selective laser ionization and electromagnetic mass separation. For the Mn and Ni experiments, the short-lived isotopes ^{56}Mn ($t_{1/2}$=2.58 h) and ^{65}Ni (2.52 h) were implanted directly. Since ISOLDE cannot produce clean beams of Fe isotopes, in order to study the lattice location of this element the short-lived precursor ^{59}Mn (4.6 s) was implanted, which decays into the long-lived ^{59}Fe (44.5 d). Note that during the decay of ^{59}Mn the ^{59}Fe daughter atoms receive on average a recoil of 200 eV, which assures that ^{59}Fe leaves the initial ^{59}Mn lattice site and comes to rest within a few interatomic distances from that position, subsequently finding its own lattice site. The implantations were carried out at room temperature (RT) under vacuum better than 10^{-5} mbar and at an angle of 17° from the [0001] surface to avoid channeling implantation and produce well-defined depth profiles. The implantation conditions as well as the resulting, approximately Gaussian depth profiles and maximum concentrations, as predicted by SRIM [16], are presented in table 1. In the case of the long-lived isotope ^{59}Fe, the complete activity required for the whole experiment was implanted in one step. In contrast, for the short lived isotopes, in case of ^{56}Mn two implantations were performed, one at the beginning of the experiment and another before the 600 °C annealing step, while for ^{65}Ni following the initial implantation more activity was added into the same spot on the sample before the 200, 300, 400, 500, 600 and 700 °C annealing steps. Detailed information about the emission channeling EC-SLI experimental apparatus can be obtained in reference [17]; typical experimental procedures for ^{56}Mn, ^{59}Fe and ^{65}Ni as well as their relevant β^- decay characteristics have been described in reference [11].

Table 1. Implantation energy and fluence for the three experiments. The corresponding projected range, straggling and TM peak concentration were calculated by SRIM [16].

TM probe	Implantation energy (keV)	Fluence (at. cm^{-2})	Projected range R_p (Å)	Straggling (Å)	Peak concentration (cm^{-2})
^{56}Mn	40	9×10^{12}	256	93	4×10^{18}
^{59}Fe	60	2×10^{13}	362	127	6×10^{18}
^{65}Ni	30	4×10^{13}	196	73	2×10^{19}

Isochronal annealing under vacuum was performed *in situ* for 10 min for each annealing step. A position-sensitive detector described in [13, 18] was used to measure the angle-dependent emission yield of electrons in the vicinity of [0001], $[\bar{1}101]$, $[\bar{2}201]$ and $[\bar{4}401]$ directions at room temperature in the as-implanted state and after each annealing step, with counting statistics of few thousand counts per pixel. The resulting emission patterns were corrected for background produced by γ-rays and β^- particles scattered by the chamber walls. By means of closing a shutter in front of the detector, the amount of background resulting from the γ-rays was estimated to be 10%. In order to assess the background of scattered electrons we used a Monte Carlo computer code based on the GEANT4 toolkit [19], that takes into account the composition and geometry of the sample, the sample holder, the detector and the major parts

of the vacuum setup. Combining both estimates showed that for ^{59}Fe only ~50% and for ^{56}Mn and ^{65}Ni ~45% of the count rate resulted from β^- particles directly emitted from the sample towards the detector. Since the remaining background events do not contribute to the measured channeling effect, the fractions of probe atoms on specific lattice sites, obtained by the fitting procedures described below, were multiplied by corresponding correction factors.
Quantitative lattice location was achieved by fitting the experimental patterns with a linear combination of theoretical patterns for TM probes on different lattice sites, using the fit procedure outlined in [13, 18]. One of the fit parameters in this procedure is a scaling factor common to all angles of a pattern, which allows normalizing the count rate of experimental patterns and displaying them as normalized yield relative to isotropic emission. The theoretical patterns were calculated using the many-beam theory of electron diffraction in single crystals [12, 13]. In these calculations the crystal potential is approximated by a superposition of atomic Doyle-Turner potentials. Since for a description of the emission channeling effect only beta particles moving under relatively small angles with respect to the channeling axis are relevant and these move at relativistic velocities, the potential along the channeling direction can be averaged and the electron wave function split into a longitudinal component along the channeling direction, which obeys a relativistic Klein-Gordon equation, and a transverse component perpendicular to the axis, which is given by the solution of a two-dimensional Schrödinger equation in a periodic potential. The beta particle flux density inside the crystal can then be calculated after obtaining the transverse electron wave function using standard Fourier decomposition and Bloch wave techniques. The many-beam approach has proven to accurately describe emission channeling effects in a multitude of cases [12, 13]. As values for the lattice constants of 6H-SiC we used a=3.081 Å and c=15.117 Å. To account for host atom lattice vibrations in the many-beam simulations we assumed root mean square (rms) Gaussian displacements from their ideal lattice sites of 0.0603 Å for Si atoms and 0.0611 Å for C atoms at room temperature. A discussion on the choice of rms displacement values, as well as details on the approximation of the continuous β^- spectra of ^{56}Mn, ^{59}Fe and ^{65}Ni, can be found in Ref. [11].

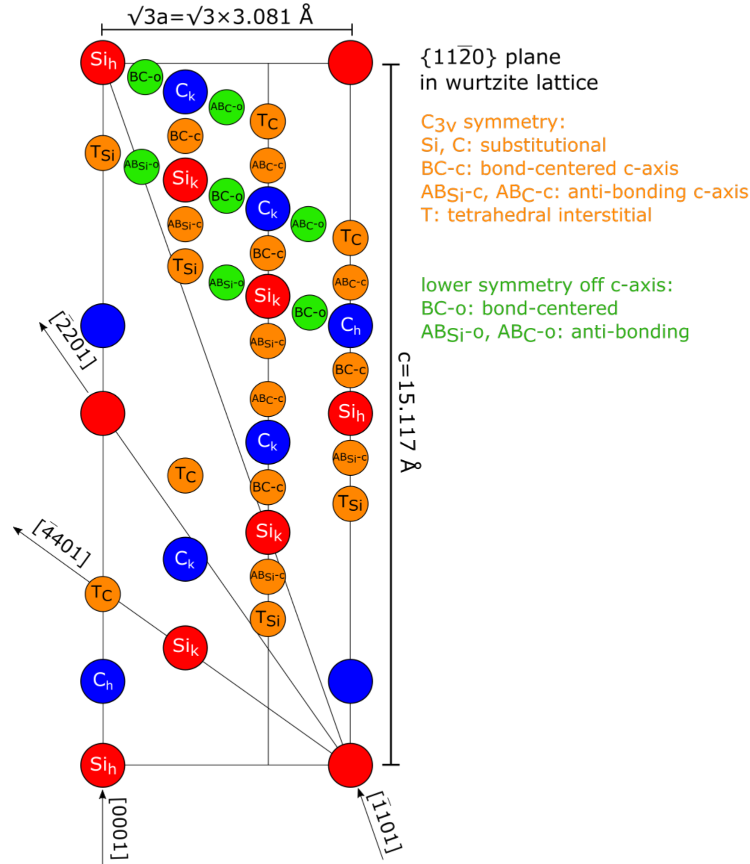

Figure 1. Positions of the major sites in the (11$\bar{2}$0) plane of the 6H-SiC lattice, showing the Si and C hexagonal-like (*h*) and cubic-like (*k*) atom positions and the major interstitial sites that were investigated as possible lattice sites of TM atoms. Note that along the [0001] direction the substitutional (S_{Si} and S_C) and tetrahedral interstitial (T_{Si} and T_C) sites are all located on the same row. The angles between the [0001] and the [$\bar{1}$101], [$\bar{2}$201] and [$\bar{4}$401] axes are 19.4°, 35.2° and 54.7°, respectively.

As described, for example, in references [4, 20], six Si-C bilayers are required to define the unit cell of the 6H polytype along the *c*-axis [0001] stacking direction, with a stacking sequence of one hexagonal (*h*) layer following two cubic (*k*) layers, i.e. one third of the Si and C atoms are in hexagonal and two thirds in cubic configurations (figure 1). Probes located on hexagonal-like (*h*) substitutional sites (either Si or C) will produce patterns that are somewhat different from probes on corresponding cubic-like (*k*) substitutional sites: the patterns for ^{59}Fe probes on substitutional Si (*h*) and (*k*) as well as a statistical mixture of both (denoted as *h*+*k*), are illustrated in figure 2. The (*h*+*k*) mixture assumes the presence of the emitters in both (*h*) and (*k*) substitutional sites with a statistical weight of 1/3 hexagonal and 2/3 cubic. In our many-beam simulations, besides the substitutional Si (S_{Si}) and C (S_C) sites in hexagonal and cubic surroundings and with varying isotropic rms displacements, we also considered the interstitial sites of highest symmetry, i.e. tetrahedral (T) and anti-bonding (AB) in both sublattices, as well as the bond-centered (BC), which are also illustrated in figure 1. In addition, we also considered displacements from ideal substitutional or major interstitial positions, however, only along the *c*-direction. In contrast to 3C-SiC, where possible displacements along <111>, <110> and <100> were investigated, many-beam simulations for displacements basal to the *c*-axis in 6H would have required excessive computational resources due to the large number of substitutional and interstitial positions in the unit cell

and the corresponding displacements. Furthermore, as described in the following, the experimental data can be well reproduced with the lattice sites considered in this work.

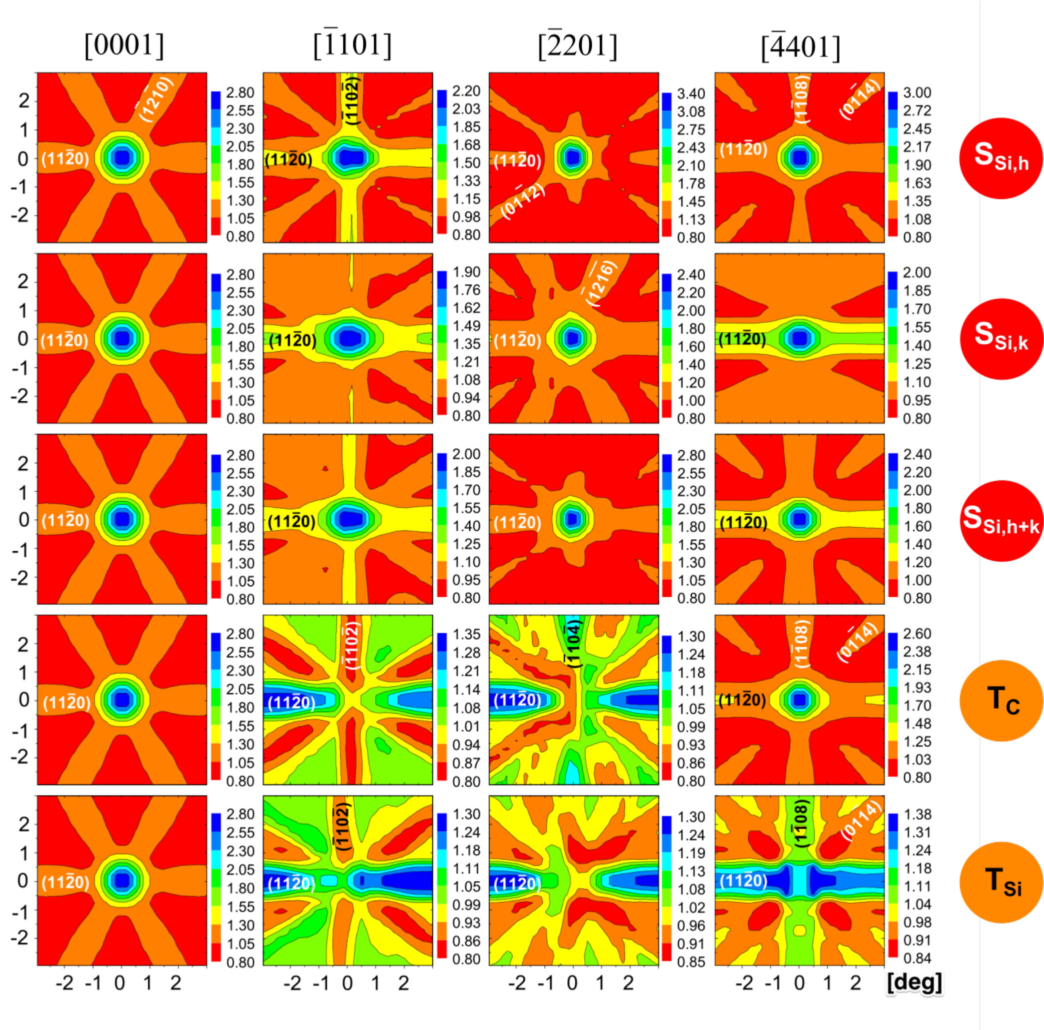

Figure 2. Theoretical ^{59}Fe β^- angular emission yield patterns within ±3° of the four major crystallographic directions as simulated for the major substitutional and interstitial sites. The four rows represent the patterns for $S_{Si,h}$ (100% of emitter atoms on substitutional Si hexagonal), $S_{Si,k}$ (100% on substitutional Si cubic), $S_{Si,h+k}$ (mixture of 33.3% hexagonal and 66.7% cubic substitutional Si), T_C (100% on tetrahedral carbon-coordinated interstitial) and T_{Si} (100% on tetrahedral silicon-coordinated interstitial) sites. These sites are identified in figure 1 and the definition of hexagonal and cubic sites can be found in [4, 20].

3. Results and discussion

Figure 2 shows the calculated β^- emission channeling patterns for ^{59}Fe on ideal substitutional (*h*), (*k*) and (*h*+*k*) Si sites and ideal tetrahedral interstitial T_C. Probes sitting at S_{Si} sites are always aligned with rows and planes of Si atoms, which cause the emitted β^- particles to be channeled. Thus, an increase in the measured β^- count rate is expected along all axial and planar directions. On the other hand, for the interstitial T_C sites, maxima in the β^- count rate are expected along those directions with which the T_C sites are aligned, and minima along those where they are centered in the interstitial region, see figures 1 and 3. For instance, T_C sites are centered within (11$\bar{2}$0) planes and rows of Si and C atoms along the [0001] direction; they are also aligned with rows of Si atoms along [$\bar{4}$401] but are completely interstitial with

respect to the [1101] and [2201] axis. This means that for T_C sites one expects to observe channeling effects along (1120), [0001] and [4401] but minima along [1101] and [2201] directions. While the theoretical emission yields from ^{56}Mn and ^{65}Ni exhibit narrower channeling effects due to the higher energies of their β^- particles, their patterns are otherwise similar to ^{59}Fe and therefore not shown here.

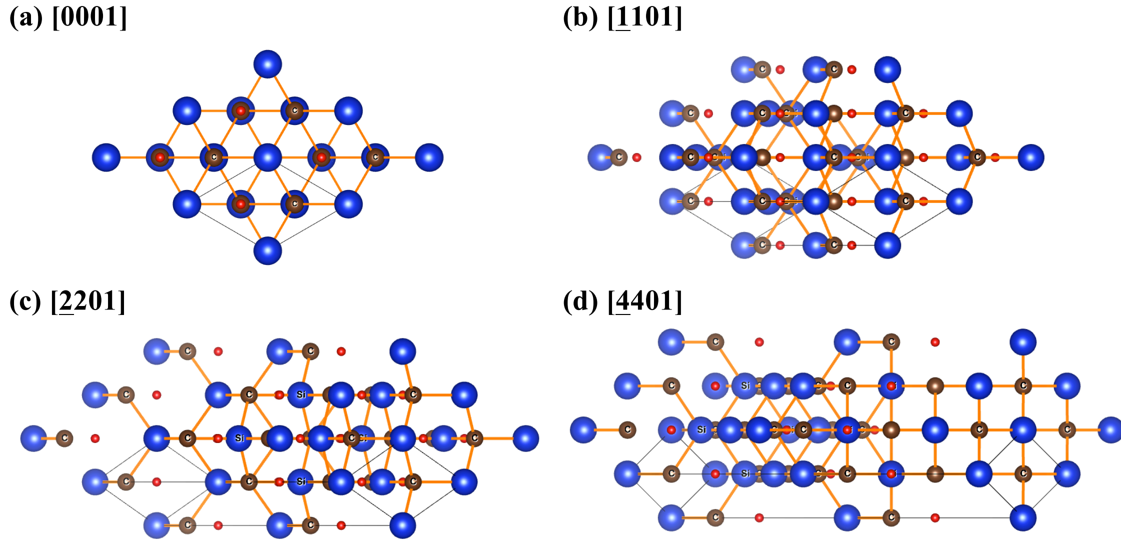

Figure 3. Schematic projections along the major crystallographic directions of a 6H-SiC crystal consisting of four unit cells. The positions of the interstitial T_C sites are shown as small red circles. The bonds between Si (in blue) and C (in brown) atoms are indicated in orange.

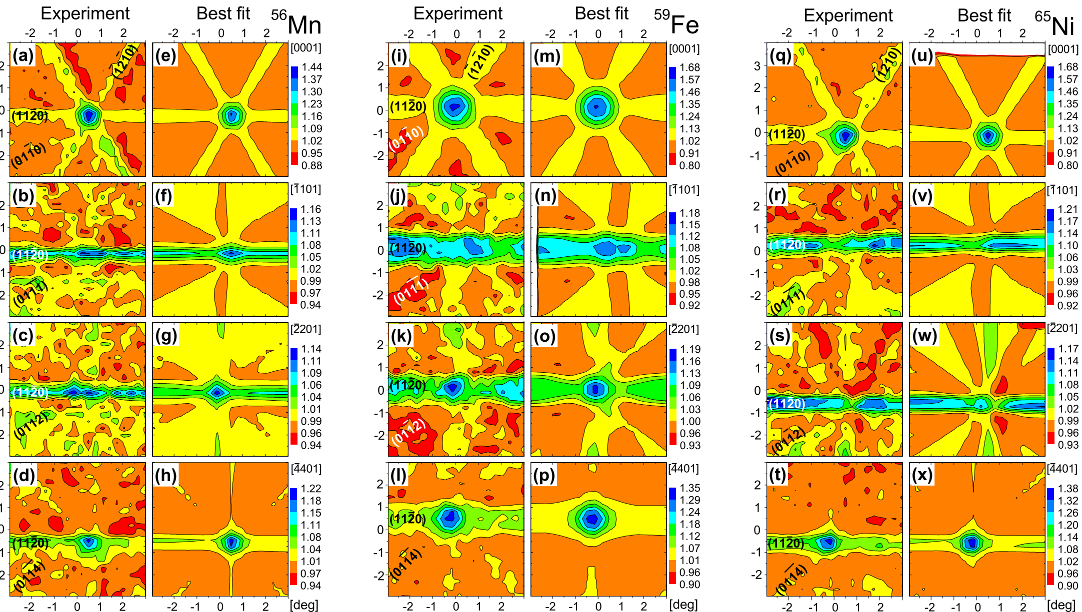

Figure 4. Normalized experimental β^- emission channeling patterns and corresponding best fits for a combination of ideal $S_{\mathrm{Si},h+k}$ and T_C sites, in the vicinity of [0001], [1101], [2201] and [4401] directions following ^{56}Mn (a)-(h), ^{59}Fe (i)-(p) and ^{65}Ni (q)-(x) implantation at room temperature.

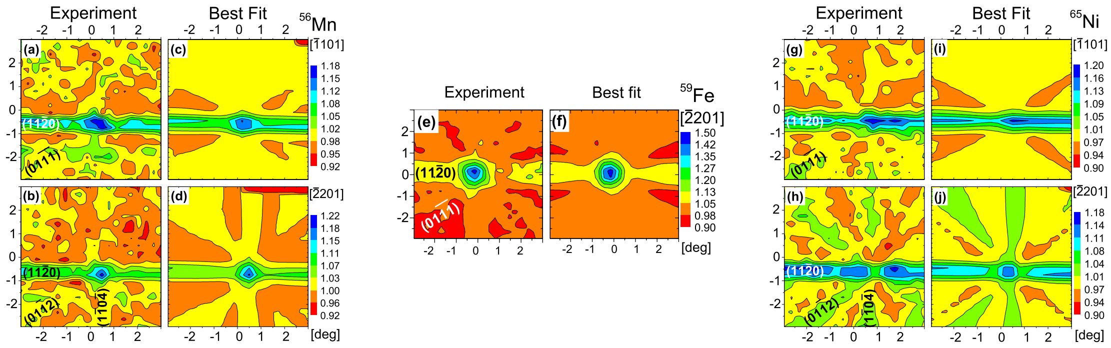

Figure 5. Normalized experimental β^- emission channeling patterns from ^{56}Mn (a),(b), and ^{65}Ni (g),(h) and corresponding best fits for a combination of ideal $S_{Si,h+k}$ and T_C sites in the vicinity of [$\bar{1}$101] and [$\bar{2}$201] directions following annealing at 400 °C. In the ^{59}Fe (e) case, the pattern was collected only in the vicinity of the [$\bar{2}$201] direction after annealing at 600 °C (e), and also the best fit (f) using the ideal-(S_{Si}+T_C) sites combination.

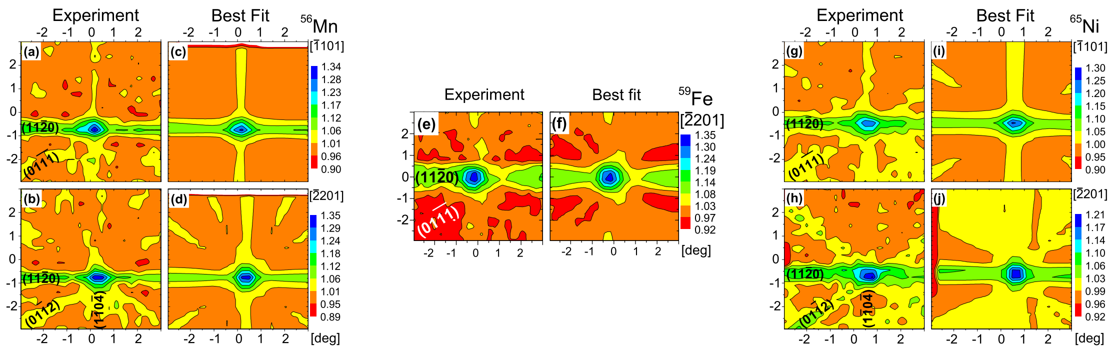

Figure 6. Normalized experimental β^- emission channeling patterns from ^{56}Mn (a),(b) and ^{65}Ni (g),(h) and corresponding best fits for a combination of ideal S_{Si} and T_C sites, in the vicinity of the [$\bar{1}$101] and [$\bar{2}$201] directions following annealing at 600 °C. In the ^{59}Fe (e) case, the β^- emission channeling pattern was collected only in the vicinity of [$\bar{2}$201] direction after annealing at 900 °C, and also the best fit (f) using the ideal-(S_{Si}+T_C) sites combination.

The normalized experimental angular-dependent β^- emission patterns for all crystallographic directions measured for the three probes in the RT as-implanted state are shown in figure 4, while figure 5 displays [$\bar{1}$101] and [$\bar{2}$201] patterns following annealing at 400 °C for Mn and Ni and at 600 °C for Fe, and figure 6 following annealing at 600 °C for Mn and Ni and at 900 °C for Fe. Direct comparison of figure 4 to the theoretical patterns in figure 2 shows that T_C sites provide the best visual match to the RT as-implanted experimental results. According to what has been said above, the T_C site preference is best visible from the [$\bar{1}$101] and [$\bar{2}$201] patterns since the T_C sites are not aligned with these directions. However, there are certain features in the experimental patterns for which a mere T_C site occupancy cannot account, in particular the fact that weak central axial peaks remain along [$\bar{1}$101] and [$\bar{2}$201] directions. A more quantitative analysis is achieved by fitting the experimental yields with linear combinations of up to three theoretical patterns from high symmetry sites plus a constant angular distribution from so-called "random sites", using the fit procedure outlined in [13,18]. Experimental channeling results can generally only be satisfactorily described if, in addition to the fractions of probe atoms on regular, high-symmetry sites, such a fraction on "random" sites is allowed. Note that the "random fraction" corresponds to probe atoms on all types of lattice sites that contribute to the angular yield in an isotropic way, e.g. isolated probe atoms

in sites of very low crystal symmetry, or probe atoms within highly damaged or even amorphous surroundings, or whose electrons are de-channeled by defects. A large random fraction may thus be the consequence of significant crystal damage from the implantation process. In the fitting process we have first considered single fractions on regular sites, to find that two main types of sites contribute to the best fits, depending on the annealing temperature. For low annealing temperatures (<400 °C) the best fits for all three investigated TMs were obtained with the tetrahedral, carbon coordinated, interstitial site T_C. For annealing temperatures above 400 °C, the best fits resulted from the probe atoms occupying ideal $S_{Si,h+k}$ sites. The next step was to allow the fitting routine to include simultaneously two ideal lattice sites. For all studied TM probes, the combination of $S_{Si,h+k}$+T_C gave the best fit and considerably improved the chi square of fit (χ^2) compared to the single fraction fit by up to 50%. Hence we found no indications that the TM site preference deviates from the statistical mixture of 1/3 (*h*) hexagonal- and 2/3 (*k*) cubic-like substitutional sites in the 6H crystal, and in the following, when S_{Si} is mentioned, we will always understand this statistical mixture of Si sites. Next, we explored the situation where more than two sites were being occupied. In particular, tetrahedral interstitial Si-coordinated (T_{Si}) and carbon substitutional S_C, either (*h*), (*k*) or a mixture of both (*h*+*k*) were used as third fraction in the fits. While this reduced χ^2 somewhat further, but always <5%, the combinations S_{Si}+T_C+T_{Si} and S_{Si}+T_C+S_C resulted in T_{Si} and S_C fractions that were close to zero or negative. Hence we conclude that large fractions on T_{Si} or S_C sites can be excluded.

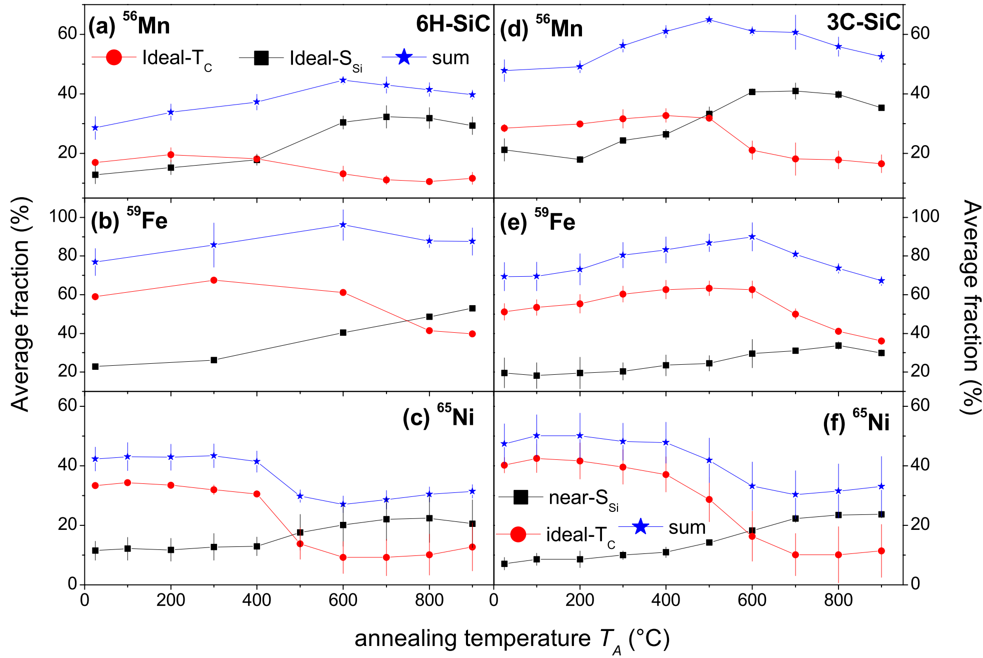

Figure 7. 6H-SiC fitted fractions of ^{56}Mn (a), ^{59}Fe (b) and ^{65}Ni (c) emitter atoms on ideal substitutional Si (in black) and ideal tetrahedral T_C sites (in red) plus the sum of both site fractions (in blue) as a function of the annealing temperature, averaged for the four measured crystallographic directions. The error bars represent the spread in fitted fractions for the different crystallographic directions. Fitted fractions for ^{56}Mn (d), ^{59}Fe (e) and ^{65}Ni (f) in 3C-SiC from previous published work [11], are also plotted for comparison. The implanted fluences for the 3C samples (2×10^{13} cm^{-2} for ^{56}Mn, 3×10^{13} cm^{-2} for ^{59}Fe and 6×10^{13} cm^{-2} for ^{65}Ni) were similar to those of the 6H experiments.

For the fraction analysis as a function of annealing temperature shown in figure 7(a)-(c), the fits were confined to the two regular lattice positions ideal interstitial T_C and ideal substitutional S_{Si}, plus random sites. While the best fit results for the TM emission channeling patterns contain always a mixture of the TM probes on these two lattice sites, the contributions change considerably as a function of annealing temperature. For the as-implanted state the best fits for the ^{56}Mn probe are shown in figures 4(e)-(h) with 17% on T_C sites and 13% on S_{Si}, in figures 4(m)-(p) for ^{59}Fe with 59% on T_C and 23% on S_{Si}, and in figures 4(u)-(x) for ^{65}Ni with 33% on T_C and 12% on S_{Si}. Hence in all three cases the T_C sites dominate in the as-implanted state and this situation remains rather unchanged for annealing up to 400 °C for Mn and Ni, and up to 600 °C for Fe, cf figures 5 and 7. With further annealing the TM fractions on T_C sites decrease whereas the fractions on Si sites increase, so that presently in the [$\bar{1}$101] and [$\bar{2}$201] patterns of figure 6 electron channeling effects are visible for all axial and planar directions.
The site fractions on interstitial T_C and substitutional Si sites which we have determined previously in 3C-SiC for the same three transition metal probes [11] are shown in figure 7 (d)-(f). As can be seen, the lattice site preferences as a function of annealing temperature are very similar for the two polytypes. In both 6H and 3C for ^{56}Mn and ^{59}Fe the sum fractions increase for annealing temperatures up to 550-600 °C, while no such increase is observed for ^{65}Ni and the sum fractions decrease simultaneously with the site change from T_C to S_{Si}. In emission channeling, growth of the sum fraction on regular sites, i.e. a reduction of the random fraction, is most commonly associated with the annealing of implantation damage. It hence seems as if this annealing was much less pronounced in the Ni-implanted samples, possibly as a consequence of the fact that they received the highest fluences and damage was more persistent against annealing. The sum of the fractions on S_{Si}+T_C sites in both ^{59}Fe experiments was a factor of 1.5-2 higher than in case of ^{56}Mn and ^{65}Ni, with ^{59}Fe sum fractions reaching above 90% at T_A=600 °C. While this could in principle be a consequence of the different chemical properties of the TMs, there may be other explanations. The total fluences of both ^{59}Fe experiments were a factor of 2-3 lower than in case of ^{65}Ni but overlapping with those of ^{56}Mn, so fluence-related effects may have played a minor role, although there must be other factors that come into play. A major difference between the ^{59}Fe and ^{56}Mn or ^{65}Ni experiments is that samples with the long-lived isotope ^{59}Fe (44.5 d) were produced via the implantation of the short-lived (4.6 s) precursor ^{59}Mn and that the samples were then stored for several weeks at RT before the measurements started. The decay of ^{59}Mn happens several seconds after the actual implantation that creates the damage in the sample. Since the ^{59}Fe nucleus receives ~200 eV of recoil, it will leave the original lattice site of ^{59}Mn and then find its new lattice site when a large part of the initial radiation damage has already been removed during the cool down of the damage cascade to RT. Further annealing may then have occurred during the prolonged sample storage at RT before the measurements started. In contrast, the short-lived probes ^{56}Mn and ^{65}Ni are directly introduced into their lattice sites during the cool-down of the damage cascade, which may favour their incorporation in sites of low symmetry that are not resolved as specific regular lattice sites in the channeling measurements and therefore form part of the "random" fraction of emitter atoms.
Due to the fact that substitutional Mn, Fe and Ni were preferentially found on the S_{Si} sites in 3C-SiC, our previous work [11] had already shown that the interaction of interstitial TMs with Si vacancies is of particular relevance and hence any mechanism that depletes or introduces V_{Si} in 6H-SiC will play also a critical role for the TM lattice site occupation. SRIM simulations [16] predict that (for a temperature of 0 K, i.e. neglecting dynamic thermal

annealing), each implanted TM ion produces around 300-400 Si vacancies and interstitials, as well as similar numbers of C-related defects. The initial vacancy distribution is approximately described by a Gaussian profile centered at somewhat more than half of the projected range of the implantation. In the following we will very briefly summarize some relevant knowledge on V_{Si} from the literature. Silicon mono-vacancies V_{Si} have been identified following irradiation of various SiC polytypes using the techniques of positron annihilation spectroscopy (PAS) [21-23] and electron paramagnetic resonance (EPR) [21, 24]. The annealing of V_{Si} occurs in various stages that seem to depend to some extent also on the polytype. In that respect, PAS found V_{Si} annealing stages at 200 °C and 800 °C in cubic [21-22] and 200 °C, 500 °C and 800 °C in hexagonal polytypes [22]. By means of EPR, V_{Si} annea1ing stages at 150 °C, 350 °C and 750 °C were observed in 3C [21], whereas for hexagonal polytypes less data seem to exist but a major stage at 750 °C is well established [25-26]. The low-temperature stages around 150-200 °C are generally interpreted as recombination of close-by V_{Si} and Si interstitials (Frenkel pairs) [21, 22, 28, 29]. In contrast, the annealing stages around 750-800 °C result from the transformation of V_{Si} into a complex defect which is believed to be $V_C C_{Si}$ [24-26]; such carbon vacancy carbon anti-site complexes have been theoretically predicted as being energetically more stable than monovacancies in *p*-type and intrinsic or compensated SiC of all polytypes [27-29]. Since irradiated SiC will eventually become compensated due to the electrical activity of deep defects, the transformation $V_{Si} \rightarrow V_C C_{Si}$ may also occur in samples that were initially *n*-type and hence be a general characteristic of heavily irradiated SiC. The activation energy for the transformation $V_{Si} \rightarrow V_C C_{Si}$ was estimated to be around ~1.8-2.5 eV [27-29].

While the increase of the TM probe fractions on ideal-Si sites as a consequence of annealing follows the decrease of the ideal-T_C fractions to some extent, the simultaneous reduction of the sum fractions means that the site changes $T_C \rightarrow S_{Si}$ coincide also with the loss of probe atoms to random sites. As we have previously outlined [11], we interpret these lattice site changes from T_C to S_{Si} and random sites as the onset of migration of interstitial TMs that may then react with V_{Si} still existing in the sample or lead to the occupation of random sites. By using simple Arrhenius models, as described e.g. in references [30-32], we can then estimate the activation energy E_M for the interstitial TM diffusion with the following formula:

$$E_{\mathrm{M}} = k_{\mathrm{B}} T \ln \left[\frac{\nu_0 \Delta t}{N \ln(f_{n-1}/f_n)} \right].$$

Here ν_0 is the migration attempt frequency, which we take as 10^{12} s^{-1}, i.e. of the order of the lattice vibrations, Δt_{ann} the annealing time, T the annealing temperature, f_n the interstitial TM fraction after annealing at T, f_{n-1} the fraction before the annealing and N the required number of steps before an interstitial TM atom combines with a silicon vacancy or reaches a random position. We consider two opposite scenarios for N: (1) an upper limit estimate for E_M is obtained if one jump is considered enough to move a TM atom into a Si vacancy or a random position; (2) reaching a lower limit estimate for E_M requires making reasonable assumptions on the maximum number of jumps N_{max} that take place before the TM_i reaches a Si vacancy or a random position. Here we assume that this is quite likely if the diffusion induced broadening of the TM depth profile would reach a value that corresponds to the projected range R_p of the implantation. This would mean that a large fraction of TM probes would reach the surface or diffuse so deep into the sample that the channeling effects would be dampened considerably due to de-channeling. Both diffusion to the surface and into the depth of the sample lead to a loss of channeling effects, which increases the random fraction in the fits and

shows as decrease in the sum fraction of emitter atoms in figure 7. We note that since such a decrease in the sum fractions is as a matter of fact observed in SiC for temperatures above 400-600°C, this scenario with N_{max} is actually not unlikely. The diffusion-induced broadening resulting from a number of N jumps can be estimated by $(r_M^2 N/3)^{1/2}$, where r_M is the mean jump width. If we assume that r_M is given by the closest distance between two interstitial C-coordinated T_C sites, which is 3.08 Å along [$\underline{2}$201] directions, one estimates N_{max} from R_p via $N_{max}=3[R_p/r_M]^2$.

Table 2 compiles our estimates for the interstitial migration energies E_M of Mn, Fe and Ni in 6H-SiC and compares them to what we previously derived for 3C-SiC. In all cases the E_M values for 6H are similar to 3C. Since the fraction of interstitial Fe decreases only at higher annealing temperatures (T_A=600-900 °C) than in the case of Mn and Ni (400-600 °C) the estimated migration energies E_M for Fe are higher than for Mn and Ni. We note that the range of TM_i migration energies overlaps with the activation energy (~1.8-2.5 eV) where the metastable Si vacancy V_{Si} supposedly converts to a complex $V_C C_{Si}$ antisite defect. As we have already previously argued in [11], the formation of this anti-site complex can hence provide an explanation why not all TMs that disappear from interstitial T_C sites are incorporated in S_{Si} sites: since TMs seem to be unable to occupy C sites, the transformation $V_{Si} \rightarrow V_C C_{Si}$ removes a major trap, so that the probes will diffuse interstitially until they form part of the random fraction by reaching sites on the surface or deep in the bulk of the sample.

Table 2. Estimates for the interstitial migration energy E_M of the TMs considering two different scenarios for the number of jumps: N=1 and $N=N_{max}$. For the last scenario, the value of N_{max} is estimated using the assumptions described in the text. We also provide the E_M values found for 3C-SiC for comparison.

	6H-SiC			3C-SiC [11]		
TM element	$E_M(N=1)$ [eV]	$E_M(N=N_{max})$ [eV]	N_{max}	$E_M(N=1)$ [eV]	$E_M(N=N_{max})$ [eV]	N_{max}
Mn	2.7	1.9	20720	2.6	1.9	
Fe	3.2	2.3	41440	3.0	2.2	≈16180
Ni	2.3	1.7	12150	2.4	1.7	

Finally, we compare the current experiments on ^{56}Mn, ^{59}Fe and ^{65}Ni in SiC to our previous lattice location results of the same TMs in Si [30-34] and to ^{59}Fe in diamond [35], i.e. the two elemental semiconductors formed by the constituents of SiC. In Si these TM probes were found to occupy three types of lattice sites: ideal substitutional sites, displaced substitutional sites and near-tetrahedral interstitial sites, with varying fractions that depended on the annealing temperature. As a general characteristic for Si, the probe atom displacements related to the displaced substitutional sites were rather large with values between 34% and 100% of the bond length of 1.176 Å. Such large displacements were interpreted as TMs incorporated in multi-vacancy complexes such as di-vacancies or hexa-vacancy rings, in which the TMs would occupy sites that are actually close to the bond-center (BC) position in an undisturbed lattice. While we tested for the existence of such displaced substitutional sites in the 3C-SiC experiment, possible values were at maximum ~25% of the bond length. Moreover, while the displacements in case of Si were either independent of or even growing with annealing temperature, in 3C-SiC they almost completely disappeared after annealing at 900 °C [11]. From this we conclude that either TMs inside multi-vacancy complexes seem to play a less prominent role in SiC than in Si, or that if TMs are incorporated in multi-vacancies in SiC they still occupy sites that are relatively close to a substitutional Si position. Another

striking difference between Si and SiC is that the type of rather simple site changes from interstitial to substitutional and random sites as function of annealing temperature, which was obvious in SiC, was probably not seen in Si since its observation would require implantations below room temperature. In Si the interstitial TMs should be diffusing so rapidly at RT that they immediately get attached to traps in the lattice, hence the interstitial TMs seen in Si were probably not free interstitials (as we assume to have seen in SiC) but bound in complexes, the nature of which is not completely clear at the moment.
In case of diamond, lattice location data only exist for ^{59}Fe [35]. In stark contrast to both SiC and Si, no interstitial Fe could be seen in diamond, whereas the type of substitutional site was similar to the case of SiC, i.e. characterized by displacements smaller than ~25% of the bond length.

4. Conclusions

We have experimentally determined the lattice location of the TM impurity probes ^{56}Mn, ^{59}Fe and ^{65}Ni in 6H-SiC as a function of annealing temperature up to 900 °C. In order to be able to distinguish between the (*h*) and (*k*) type substitutional sites and a variety of interstitial positions, we have incorporated the 6H structure into the many-beam simulation code. This should also pave the way for further lattice location studies in this structure, since 6H-SiC is one of the most used polytypes in high power semiconductor industry.
Similar to our recent results on 3C-SiC [11], the TM impurities are preferentially located on interstitial T_C and substitutional Si sites. We found no indications for a deviation of the TM distribution on the substitutional Si sites from the statistical mixture of 1/3 hexagonally (*h*) and 2/3 cubically (*k*) coordinated positions. The interstitial TM migration energies E_M were estimated as 1.7-2.7 eV for Mn and Ni, and 2.3-3.2 eV for Fe. These values are comparable to those previously determined for 3C-SiC. At the highest annealing temperatures the TM atoms increasingly populate random sites in both 6H and 3C-SiC. Consequently, we consider that the transformation of V_{Si} to the $V_C C_{Si}$ complex is as important for TMs in the 6H as in the 3C polytype and provides in both cases a possible explanation of why silicon vacancies are unavailable as major traps following annealing at higher temperatures. Overall we have found no indication that the wider band gap and the existence of hexagonally and cubically coordinated sites in 6H-SiC alter the behaviour of implanted transition metals in comparison to its cubic 3C counterpart.

Acknowledgments
We acknowledge the beam time provided by the ISOLDE collaboration. This work was funded by the Portuguese Foundation for Science and Technology (FCT) through project CERN/FIS-NUC/0004/2015 and the strategic project UID/Multi/04349/2013, by the FWO Vlaanderen and the KU Leuven (STRT/14/002 and GOA/14/007). ARG Costa is thankful for FCT grant SFRH/BD/86386/2012. The ISOLDE beam times were supported by the European Commission through the Horizon 2020 program (grant number 654002 ENSAR2).

References

[1] Trew R J, Yan J B and Mock P M 1991 The potential of diamond and SiC electronic devices for microwave and millimeter-wave power applications *Proc. IEEE* **79** 598-620
[2] Neudeck P G 1994 Progress towards high temperature, high power SiC devices *Inst. Phys.: Conf. Ser.* **141** 1-6
[3] Johnson C, Wright N, Uren M, Hilton K, Rahimo M, Hinchley D, Knights A, Morrison D,

Horsfall A, Ortolland S and O'Neill A 2001 Recent progress and current issues in SiC semiconductor devices for power applications *IEEE Proc. - Circuits, Devices Syst.* **148** 101-8

[4] Lebedev A A 2006 Heterojunctions and superlattices based on silicon carbide *Semicond. Sci. Technol.* **21** R17-34

[5] Wright N G, Horsfall A B and Vassilevski K 2008 Prospects for SiC electronics and sensors *Mater. Today* **11** 16-21

[6] Kimoto T 2015 Material science and device physics in SiC technology for high-voltage power devices *Jpn. J. Appl. Phys.* **54** 040103

[7] Ferro G 2015 3C-SiC heteroepitaxial growth on silicon: The quest for holy grail *Critical Reviews in Solid State and Materials Sciences* **40** 56-76

[8] Ikeda M, Matsunami H and Tanaka T 1980 Site effect on the impurity levels in 4H, 6H, and 15R SiC *Phys. Rev.* B **22** 2842-54

[9] Schneider J. and Maier K. 1993 Point defects in silicon carbide *Physica* B 185 199-206

[10] Lebedev A A 1999 Deep level centers in silicon carbide: A review *Semiconductors* 33 107-30

[11] Costa A R G, Wahl U, Correia J G, Bosne E, Amorim L M, Augustyns V, Silva D J, Silva M R and Pereira L M C 2017 Lattice location of implanted transition metals in 3C-SiC *J. Phys D: Appl. Phys* **50** 215101

[12] Hofsäss H and Lindner G 1991 Emission channeling and blocking *Phys. Rep.* **201** 121-83

[13] Wahl U 2000 Advances in electron emission channeling measurements in semiconductors *Hyperfine Interact.* **129** 349-70

[14] Vetter U, Hofsäss H, Wahl U and Dietrich M 2003 Lattice location studies of rare earth impurities in 3C-, 4H- and 6H-SiC *Diam. Relat. Mater.* **12** 1883-6

[15] Jonson B and Richter A 2000 More than three decades of ISOLDE physics *Hyperfine Interact.* **129** 1-22

[16] Ziegler J F, Ziegler M D and Biersack J P 2010 SRIM - The stopping and range of ions in matter (2010) *Nucl. Instruments Methods Phys. Res.* B **268** 1818-23

[17] Silva M R, Wahl U, Correia J G, Amorim L M and Pereira L M C 2013 A versatile apparatus for on-line emission channeling experiments *Rev. Sci. Instrum.* **84** 073506

[18] Wahl U, Correia J G, Czermak A, Jahn S G, Jalocha P, Marques J G, Rudge A, Schopper F, Soares J C, Vantomme A and Weilhammer P 2004 Position-sensitive Si pad detectors for electron emission channeling experiments *Nucl. Instruments Methods Phys. Res.* A **524** 245-56

[19] Agostinelli S *et al* 2003 GEANT4 - A simulation toolkit *Nucl. Instruments Methods Phys. Res.* A **506** 250-303

[20] Capitani G C, Di Pierro S and Tempesta G 2007 The 6H-SiC structure model: Further refinement from SCXRD data from a terrestrial moissanite *Am. Mineral.* **92** 403-7

[21] Itoh H, Kawasuso A, Ohshima T, Yoshikawa M, Nashiyama I, Tanigawa S, Misawa S, Okumura H and Yoshida S 1997 Intrinsic defects in cubic silicon carbide *Phys. Status Solidi* a **162** 173-98

[22] Kawasuso A, Weidner M, Redmann F, Frank T, Sperr P, Kögel G, Yoshikawa M, Itoh H, Krause-Rehberg R, Triftshäuser W and Pensl G 2004 Vacancy Defects Detected by Positron Annihilation *Silicon carbide: Recent major advances* eds W J Choyke, H Matsunami and G Pensl (Berlin, Heidelberg: Springer) pp 563-584

[23] Kawasuso A, Chiba T and Higuchi T 2005 Angular correlation of annihilation radiation associated with vacancy defects in electron-irradiated 6H-SiC *Phys. Rev.* B **71** 193204

[24] Son N T, Wagner M, Hemmingsson C G, Storasta L, Magnusson B, Chen W M, Greulich-Weber S, Spaeth J M and Janzén E 2004 Electronic structure of deep defects in SiC *Silicon carbide: Recent major advances* eds W J Choyke, H Matsunami and G Pensl (Berlin, Heidelberg: Springer) pp 461-492

[25] Lingner T, Greulich-Weber A, Spaeth J M, Gerstmann U, Rauls E, Hajnal Z, Frauenheim T and Overhof H 2004 Structure of the silicon vacancy in 6H-SiC after annealing identified as the carbon vacancy-carbon antisite pair *Phys. Rev.* B **64** 245212

[26] Pinheiro M V B, Rauls E, Gerstmann U, Greulich-Weber S, Overhof H and Spaeth J M 2004 Silicon vacancy annealing and D_{I} luminescence in 6H-SiC *Phys. Rev.* B **70** 245204

[27] Rauls E, Lingner T, Hajnal Z, Greulich-Weber S, Frauenheim T and Spaeth J M 2000 Metastability of the Neutral Silicon Vacancy in 4H-SiC *Phys. Status Sol.* b **217** R1-3

[28] Bockstedte M, Mattausch A and Pankratov O 2004 Ab initio study of the annealing of vacancies and interstitials in cubic SiC: Vacancy-interstitial recombination and aggregation of carbon interstitials *Phys. Rev.* B **69** 235202

[29] Bockstedte M, Mattausch A and Pankratov O 2004 Defect Migration and Annealing Mechanisms *Silicon carbide: Recent major advances* eds W J Choyke, H Matsunami and G Pensl (Berlin, Heidelberg: Springer) pp 27-55

[30] Wahl U, Correia J G, Rita E, Araújo J P and Soares J C 2006 Fe and Cu in Si: Lattice sites and trapping at implantation-related defects *Nucl. Instruments Methods Phys. Res.* B **253** 167-71

[31] Silva D J, Wahl U, Correia J G and Araujo J P 2013 Influence of n^+ and p^+ doping on the lattice sites of implanted Fe in Si *J. Appl. Phys.* **114** 103503

[32] Silva D J, Wahl U, Correia J G, Pereira L M C, Amorim L M, Da Silva M R, Bosne E and Araújo J P 2014 Lattice location and thermal stability of implanted nickel in silicon studied by on-line emission channeling *J. Appl. Phys.* **115** 023504

[33] Wahl U, Correia J G, Rita E, Araújo J P and Soares J C 2005 Lattice sites of implanted Fe in Si *Phys. Rev.* B **72** 014115

[34] Silva D J, Wahl U, Correia J G, Amorim L M, Silva M R, Pereira L M C and Araújo J P 2016 Direct observation of the lattice sites of implanted manganese in silicon *Appl. Phys.* A **122** 241

[35] Bharuth-Ram K, Wahl U and Correia J G 2003 Lattice location of Fe in diamond *Nucl. Instruments Methods Phys. Res.* B **206** 941-6.